Journal of
Mechanics of
Materials and Structures

PLANAR GRAINED STRUCTURES WITH
TRACTION-SMOOTHING INCLUSIONS: AN ELASTOSTATIC
NUMERICAL ANALYSIS FOR SHEAR AND TORSION

Shmuel Vigdergauz

msp

PLANAR GRAINED STRUCTURES WITH TRACTION-SMOOTHING INCLUSIONS: AN ELASTOSTATIC NUMERICAL ANALYSIS FOR SHEAR AND TORSION

SHMUEL VIGDERGAUZ

The topical problem of optimizing the stress state in a bimaterial plate by proper shaping of the matrix/inclusion interface is considered with respect to a recently advanced criterion of minimizing the global variations of the contact stresses. Mathematically, the variations provide an integral-type assessment of the local stresses which requires less computational effort than direct minimization of the stress concentration factor. The proposed criterion can thus be easily incorporated in the numerical optimization scheme previously proposed by the author for similar inverse problems. It consists of an efficient complex-valued direct solver and an ordinary evolutionary search enhanced with an economical shape parametrization tool. The attendant problem of optimizing the effective shear moduli is also solved for comparison purposes. Though methodologically the paper continues the previous works of the author, the primary emphasis is now placed on developing a systematic optimization approach to obtain comprehensive numerical results for nonbiaxial loadings. This setup is of special interest since it differs drastically from the biaxial case, where the analytically known equistress interfaces serve as an efficient benchmark for both theory and computations. Consequently, given the lack of structurally specific analytical assessments, the simulations performed for a wide range of values of the governing parameters provide detailed numerical insight into the chosen case. The elastic behavior of the optimal square-symmetric structures with strongly contrasting well-ordered constituents is conveniently detailed in a set of figures.

1. Introduction

An infinite plate with a regular lattice of perfectly bonded foreign inclusions is often employed as a simple and efficient theoretical model to numerically simulate the linear elastic behavior of fibrous composites with negligible end effects. The assumed periodicity permits a statistically correct assessment of real materials with technologically inevitable small structural deviations in inclusions' shapes, sizes, and locations within the lattice cells. Mathematically, the periodicity is incorporated either in the boundary conditions on the cell sides (in FEM-like methods) or through quasiperiodic functions in the complex-variable technique. Both approaches lead to equivalent boundary-value problems for determining the stress-strain state of the cell which depend on the phases' elastic moduli and volume fractions as well as on the inclusion shape. In practical applications, the shape is much less important than the other factors and hence may be additionally used for optimizing the structure's elastic response to an applied static load.

The corresponding optimization criteria are generally distinguished as either local (like the stress concentration) or integral (like the effective moduli (EMs), whose precise definition can be found elsewhere (see, for example, [Milton 2002])). Due to their averaging nature, integral-type criteria are computationally more tractable for both perforated [Vigdergauz 2001] and bimaterial composites [Vigdergauz 2013].

While very helpful in structural engineering, the EMs provide no information on the local stresses since they involve only cell averages of the elastic field. For this reason, even though the inclusion shape results in an acceptable value of either EM, it may induce potentially damaging stress concentrations.

The direct localization and minimization of the stress peaks is hard to tackle numerically. Matters can be simplified by relaxing the optimality criterion: instead of minimizing the stress peaks we propose [Vigdergauz 2013] to minimize the *variations* of the traction stresses $\sigma_{nn}(t)$ and $\sigma_{n\theta}(t)$ in the local curvilinear coordinates $t = (n, \theta)$ along the interface L:

$$V[\sigma_{nn}] + V[\sigma_{n\theta}] \xrightarrow[\{L\}]{} \min . \tag{1-1}$$

Conforming with the theory of real-valued functions [Natanson 1955], the variations are defined through the nonnegative discrete sums of absolute values of the differences of the stresses between each two adjacent points on L:

$$V[\sigma(L)] = \sup \sum_{i=0}^{n} |\sigma(t_{i+1}) - \sigma(t_i)| \geq 0, \quad \{t_i\} \in L, \tag{1-2}$$

where the supremum is taken over all possible partitions of L with an arbitrary system of points $t_0, t_1, \ldots, t_n$ ordered by a chosen direction of traversing. For a closed contour we require $t_n = t_0$. The abstract notation σ stands here for either σ_{nn} or $\sigma_{n\theta}$

The variations are an integral measure of how the function is everywhere close to uniformity; hence (1-1) and (1-2)) provide the best possible tool to smooth the tractions.

Evidently, the V-functional is absolutely bounded below by zero. It is minimized over a set of closed continuous shapes with neither self-intersections nor angles, which may only hinder the smoothing of the tractions.

In contrast to the EM-related two-dimensional averaging of the stresses, the V-criterion is only one-dimensional and would thus be expected to have better equalizing capability in numerical simulations. On the theoretical side, this expectation is supported by the benchmark inequality [Natanson 1955],

$$V[\sigma] \geq \max(\sigma) - \min(\sigma) > 0, \quad \max(\sigma) \neq \min(\sigma), \tag{1-3}$$

which shows that V-minimization necessarily narrows the gap between the extrema of the function.

Similarly, the identity [Natanson 1955]

$$V[\sigma] = \int_L |\sigma'(t)| \, dt \tag{1-4}$$

indicates the potential capability of the V-criterion to filter computationally induced noise (stress oscillations) in points with large absolute values of the first derivative $|\sigma'(t)|$. Both above-described features do show up in the numerical simulations (see Section 5).

Though the other pros and cons of the devised criterion are detailed in [Vigdergauz 2013], we summarize them here again for completeness. The pros are as follows:

- The *V*-criterion is evidently attainable under very broad assumptions and regains equistressness, whenever such exists.

- The contact stresses in (1-1) are mutual for both phases, thus simultaneously involving them in the optimization process.

- The proposed integral-type assessment of the local stresses is more numerically stable than their direct minimization, which often presents a nasty computational problem.

- The current *V*-criterion is intimately related to the *V*-minimization of the hoop stresses along traction-free holes advanced and applied to perforated structures in [Vigdergauz 2012a; 2012b]. This allows for using the same numerical optimization scheme, as before, specifically adjusted for the current purposes.

- Numerical results (Section 5) show that minimization of the variation of the stresses does effectively smooth them. The strong filtering capability of the proposed *V*-criterion is critical for achieving our ends.

The cons:

- The proposed criterion actually defines myriads of functions, all of which behave differently within the same strictly positive minimum value of *V*. Though the numerical scheme stably identifies a single and physically sensible solution (see Section 5), in the chosen examples this may not always be the case.

- The question remains open as to how *V*-minimization affects the local criterion of the boundary stresses maxima; in other words, whether both criteria are minimized in parallel or only at the expense of each other, with the lesser maximum inducing a more rigidity-favorable stress distribution. Since the stress cell averages are fixed by a given external load (see (2-8) in the next section), the latter case seems hardly to be expected, as also illustrated in Section 5. Nevertheless, a thorough analysis is required in the future.

In the previous paper [Vigdergauz 2013], the *V*-criterion is numerically applied to identify the optimal shapes for the square checkerboard arrangement of the inclusions and biaxial loading. This combination allows us to assess the deviation of the inclusion shape from the analytical equistress optimum (see, for instance, [Milton 2002]) under geometric bounds within a periodicity cell. When the shape evolution with the increasing volume fraction c_1 is unbounded, the equistress inclusions are known to exist at any $c_1 < 1$ with the following attaining the absolute minimum in (1-1):

$$\sigma_{nn}(t) = \text{Const.} \neq 0, \quad \sigma_{n\theta}(t) = 0, \quad t \in L \quad \longrightarrow \quad V[\sigma] = 0. \tag{1-5}$$

In contrast, this paper focuses on shape *V*-optimization in an *unbounded* square lattice under *shear or torsion* when the equistress inclusions cease to exist at all and the *V*-criterion remains perhaps the only optimization measure of the local stresses. This distinction between the two problems is substantial enough for studying the shear/torsion case in its own right with the aim of augmenting the numerical application of the *V*-criterion.

In order to numerically find the *V*-optimal shapes and related quantities, we employ the same solution strategy which has been proven to be efficient in the closely related optimization problems [Vigdergauz 2012a; 2012b; 2013]. This includes an efficient complex-valued direct solver and a standard evolutionary optimization algorithm enhanced with an economical shape parametrization tool.

Our contribution is thus in extending the *V*-criterion to shear and torsion loads and in obtaining a variety of numerical results, which turn out to be drastically different from those for the biaxial case. While the stress-smoothing concept is not yet fully validated, it provides a quantitative insight into the optimal design of two-dimensional elastic structures.

The paper is organized as follows. For reader convenience, Section 2 summarizes the analytical basics required for further development. In these terms, Section 3 formulates the optimization problem and briefly sketches the applied numerical scheme. Section 4 verifies this scheme's performance against the available data in the literature. The results for the representative test cases within a wide range of governing parameters are displayed and analyzed at length in Section 5. Finally, Section 6 gives conclusions and discusses open issues.

2. Problem setup and cell governing equations

Geometrically, a two-dimensional grained regular structure with four-fold rotational symmetry is formed by replicating a basic square cell along the axes of a complex Cartesian plane $z = x + iy$, with periods ω_1 and $\omega_2 = i\omega_1$, $\operatorname{Im}\omega_1$ and $\operatorname{Re}\omega_2$ both equal to zero, and area $F = -i\omega_1\omega_2$. Let the cell contain only one inclusion perfectly bonded with the matrix along the smooth interface L, let the cell and the inclusion both be centered at the origin, and let the inclusion have at least the same square symmetry as the cell. Under these conditions, the set Λ of admissible structures is completely defined by the inclusion shape: $\Lambda = \Lambda(L)$. We adopt the index $j = 1, 2$ to identify the inclusion and the matrix, respectively. The curve L divides the cell domain S in two parts, S_1 and $S_2 = S \backslash S_1$, of the volume fractions c_1 and $c_2 = 1 - c_1$, each occupied by its own homogeneous and isotropic linearly elastic phase, with planar bulk and shear moduli K_j and μ_j, respectively.

For an applied static load, the inclusion-distorted stress tensor $\sigma(z) = \{\sigma_{xx}, \sigma_{yy}, \sigma_{xy}\}$ at any point in S is linearly given by the two Kolosov–Muskhelishvili (KM) potentials $\varphi(z)$, and $\chi(z)$ [Muskhelishvili 1975], modified in [Vigdergauz 1999] for doubly periodic problems. They are sectionally holomorphic functions [Gakhov 1966] in S:

$$\varphi(z) = \begin{cases} \varphi_1(z), & z \in S_1, \\ \varphi_2(z), & z \in S_2, \end{cases} \qquad \psi(z) = \begin{cases} \chi_1(z), & z \in S_1, \\ \chi_2(z), & z \in S_2, \end{cases} \tag{2-1}$$

where the pairs $(\varphi_1(z), \chi_1(z))$ and $(\varphi_2(z), \chi_2(z))$ are analytic, respectively, in the subdomains S_1 and S_2 of constancy of the elastic moduli.

The stresses in either subdomain take then the form

$$\operatorname{Tr}\{\sigma(z)\} = \sigma_{xx}(z) + \sigma_{yy}(z) = 4\operatorname{Re}\varphi_j'(z), \quad z \in S_j + L, \quad j = 1, 2, \tag{2-2a}$$

$$\operatorname{Dev}\{\sigma(z)\} = \sigma_{yy}(z) - \sigma_{xx}(z) = 2\operatorname{Re}[\bar{z}\varphi_j''(z) + \chi_j'(z) - \delta_{j,2}\phi'(z)], \tag{2-2b}$$

$$\sigma_{xy}(z) = \operatorname{Im}[\bar{z}\varphi''(z) + \psi'(z) + \chi_j'(z) - \delta_{j,2}\phi'(z)] \tag{2-2c}$$

$$\phi'(z) = \zeta_0(z)\varphi'(z). \tag{2-2d}$$

Here $\delta_{j,2}$ is the Kronecker delta and $\zeta_0(z)$ is the normalized quasiperiodic Weierstrass zeta function [Abramowitz and Stegun 1965]:

$$\zeta_0(z) = (F/\pi)\zeta(z), \quad [\zeta_0(z)]_m = \bar{\omega}_l, \quad l = 1, 2, \tag{2-3}$$

which implicitly incorporates the cell-type specifics. The square brackets denote the quasiperiod of the bracketed function, that is, the difference of its values at arbitrary congruent points: $[f(z)]_l \equiv f(z + \omega_l) - f(z)$, $[z]_l = \omega_l$, $l = 1, 2$.

The KM matrix-related components $\varphi_2(z)$ and $\chi_2(z)$ are also quasiperiodic and have the following form [Vigdergauz 1999]:

$$\varphi_2(z) = D_1 z + D_2 \zeta_0(z) + \xi(z), \tag{2-4a}$$

$$\chi_2(z) = R_1 z + R_2 \zeta_0(z) + \eta(z), \tag{2-4b}$$

where D_l and R_l, $l = 1, 2$, are unknown quasiperiods, $[\varphi_2(z)]_l = D_1 \omega_l + D_2 \bar{\omega}_l$ and $[\chi_2(z)]_l = R_1 \omega_l + R_2 \bar{\omega}_l$, $l = 1, 2$, and $\xi(z)$ and $\eta(z)$ are new doubly periodic functions.

Furthermore, the contact tractions $P(t) = P_x(t) + i P_y(t)$, $t \in L$, acting on either side of the interface in the normal direction $\mathbf{n} = (n, \theta)$, $0 \le \theta = \arg(t) \le 2\pi$, are obtained [Muskhelishvili 1975] by integrating the tensor product $\sigma(t) \otimes \mathbf{n} \equiv \sigma_{nn}(t) + i\sigma_{n\theta}(t)$:

$$\sigma(z) \otimes \mathbf{n} = 2\operatorname{Re}\varphi_j'(t) + \frac{d\bar{t}}{dt}[t\overline{\varphi_j''(t)} + \overline{\chi_j'(t)} - \delta_{j,2}\overline{\phi'(t)}], \tag{2-5}$$

over an arc $\gamma \in L$. From (2-2)–(2-5) we have (up to an additive constant)

$$P(t) = \int_\gamma (\sigma_{nn}(t) + i\sigma_{n\tau}(t))\, dt = \varphi_j(t) + t\overline{\varphi_j'(z)} + \overline{\chi_j(t)} - \delta_{j,2}\overline{\phi(t)}. \tag{2-6}$$

Displacements $u_n(t)$ and $u_\theta(t)$ along γ are expressed through the same functions [Muskhelishvili 1975]:

$$2\mu_j[u_n(t) + iu_\theta(t)] = \lambda_j\varphi_j(t) - t\overline{\varphi_j'(z)} - \overline{\chi_j(t)} + \delta_{j,2}\overline{\phi(t)}, \quad \lambda_j = (3 - \nu_j)/(1 + \nu_j). \tag{2-7}$$

Quasiperiods from (2-4) enter linearly into the stress averages $\langle \cdot \rangle$ over the cell (see [Vigdergauz 1999]), namely

$$\langle \operatorname{Tr} \rangle = \langle \sigma_{xx} + \sigma_{yy} \rangle = 4\operatorname{Re}(D_1 + R_2), \tag{2-8a}$$

$$\langle \operatorname{Dev} \rangle = \langle \sigma_{xx} - \sigma_{yy} \rangle = 2\operatorname{Re}(D_2 + R_1), \tag{2-8b}$$

$$\langle \sigma_{xy} \rangle = \operatorname{Im}(D_2 - R_1), \tag{2-8c}$$

which are used in the periodic problems as a given external load. They may be conveniently combined into the linearly independent trial loads:

$$\langle \operatorname{Tr} \rangle = 1, \quad \langle \operatorname{Dev} \rangle = 0, \quad \langle \sigma_{xy} \rangle = 0, \quad \text{bulk load,} \tag{2-9a}$$

$$\langle \operatorname{Tr} \rangle = 0, \quad \langle \operatorname{Dev} \rangle = 1, \quad \langle \sigma_{xy} \rangle = 0, \quad \text{shear,} \tag{2-9b}$$

$$\langle \operatorname{Tr} \rangle = 0, \quad \langle \operatorname{Dev} \rangle = 0, \quad \langle \sigma_{xy} \rangle = 1, \quad \text{torsion.} \tag{2-9c}$$

For further use we also display the $\varphi(z)$ series expansions

$$\varphi_1(z) = \sum_{k=1}^{\infty} d_1^{(k)} z^k, \quad z \in S_1 + L; \quad \xi(z) = \sum_{k=1}^{\infty} d_2^{(k)} \zeta_0^{(k)}(z); \quad \zeta_0^{(k)}(z) \equiv \frac{d^k \zeta_0(z)}{dz^k}; \tag{2-10}$$

converging for a rather smooth shape L. However, in computations they may cause spurious stress oscillations which are effectively filtered by the V-criterion, whose smoothing capability counts strongly in its favor.

Remark. Since the cell type completely resides in the Weierstrass zeta function and its derivatives, the above-sketched analytical technique holds for a general parallelogram cell. However, as stated before, we restrict ourselves to the square to reduce the computational size of the problem by employing high rotational symmetry.

Indeed, under nonbiaxial loads (2-9b) and (2-9c) the KM potentials exhibit the following properties when reflected over the x-axis ($z \to \bar{z}$) or rotated through 90 degrees ($z \to iz$) about the origin:

$$\varphi(\bar{z}) = \pm\overline{\varphi(z)}, \quad \varphi(iz) = -i\varphi(iz), \qquad \chi(\bar{z}) = \pm\overline{\chi(z)}, \quad \chi(iz) = i\chi(iz), \qquad z \in S, \tag{2-11}$$

where the upper and lowers signs (when present) correspond to shear and torsion, respectively. As a result, the coefficients $\{d_{1,2}\}$ partially vanish:

$$d_{1,2}^{(k)} = 0 \quad \text{for} \quad k \neq 4l - 2, \quad l = 1, 2, \dots, \tag{2-12}$$

while the nonzero items are either real or pure imaginary:

$$\operatorname{Im} d_{1,2}^{(4l-2)} = 0 \text{ for shear}, \quad \operatorname{Re} d_{1,2}^{(4l-2)} = 0 \text{ for torsion}, \tag{2-13}$$

and, furthermore, in view of (2-2) and (2-5):

$$\sigma_{nn}(\theta + \pi/4) = \mp\sigma_{nn}(\theta - \pi/4), \quad \sigma_{n\theta}(\theta + \pi/4) = \pm\sigma_{n\theta}(\theta - \pi/4), \tag{2-14a}$$

$$\sigma_{\theta\theta}^{(m)}(\theta + \pi/4) = \mp\sigma_{\theta\theta}^{(m)}(\theta - \pi/4), \quad \sigma_{\theta\theta}^{(i)}(\theta + \pi/4) = \mp\sigma_{\theta\theta}^{(i)}(\theta - \pi/4). \tag{2-14b}$$

With (2-11)–(2-13), the simulations can be performed only along the irreducible interval $[0, \pi/4]$ of the optimized square-symmetric interface.

The KM phase-related components are linked at the boundary L by the assumed continuity of the tractions (2-6) and displacements: (2-7)

$$\overline{\varphi_2(t)} + \bar{t}\varphi_2'(t) + \chi_2(t) - \phi(t) = \overline{\varphi_1(t)} + \bar{t}\varphi_1'(t) + \psi_1(t), \tag{2-15a}$$

$$\mu_{12}[\lambda_2\overline{\varphi_2(t)} - (\bar{t})\varphi_2'(t) - \chi_2(t) + \phi(t)] = \lambda_1\overline{\varphi_1(t)} - \bar{t}\varphi_1'(t) - \psi_1(t), \tag{2-15b}$$

$$\mu_{12} = \mu_1/\mu_2, \quad \mu_2 \neq 0, \quad t \in L.$$

Together with nonhomogeneous average loads (2-8), the boundary conditions (2-15) form the direct elastostatic problem (DEP) in finding the local stress tensor (2-2) and all the related quantities through the quasiperiodic KM potentials (2-4) in the form (2-10).

In particular, after appropriately combining identities (2-15), the traction stresses in (2-6) are [Vigdergauz 2013]

$$(1 - \mu_{12})P'(z) = (1 - \mu_{12})(\sigma_{nn}(t) + i\sigma_{n\tau}(t)) = (\lambda_1 + 1)\varphi_1'(t) - \mu_{12}(\lambda_2 + 1)\varphi_2'(t), \quad t \in L, \quad (2\text{-}16)$$

and, furthermore, with the invariant (2-2a), the hoop stresses on either side of the interface takes the form

$$\sigma_{\theta\theta}^{(j)}(t) = 4 \operatorname{Re} \varphi_j(z) - \sigma_{nn}(t), \quad t \in L, \quad j = 1, 2. \quad (2\text{-}17)$$

The analytical averaging of the local strain/stress field (2-2) while making use of (2-16) and (2-8) gives [Vigdergauz 1999] the closed expressions for the inverses of all effective moduli of the composite. Similarly to the stress averages (2-8), they linearly involve the quasiperiods D_1 and D_2 of $\varphi_2(z)$:

$$\frac{1}{K^*} = \frac{1}{K_2} + 4Aq, \quad A = 4 \operatorname{Re} D_1 - 1, \quad q = \frac{1}{K_2} + \frac{1}{\mu_2}, \quad (2\text{-}18a)$$

$$\frac{1}{\mu_1^*} = \frac{1}{\mu_2} + 4B_1q, \quad B_1 = -4 \operatorname{Re} D_2, \quad (2\text{-}18b)$$

$$\frac{1}{\mu_2^*} = \frac{1}{\mu_2} + 4B_2q, \quad B_2 = 2 \operatorname{Im} D_2, \quad (2\text{-}18c)$$

taken from the DEP solutions at the corresponding trial loads (2-9). For an alternative derivation in the case of perforated plates, see [Lukkassen et al. 2012]. The perturbation-like forms (2-18) are especially amenable to numerical evaluation, since all the structure-specific features completely reside in the coefficients:

$$D_{1,2}, R_{1,2} = D_{1,2}, R_{1,2}(K_1, K_2, \mu_1, \mu_2, c_1, L). \quad (2\text{-}19)$$

In particular, for perforated plates ($K_1, \mu_1 = 0$) we have [Vigdergauz 1999]

$$D_{1,2}, R_{1,2} = D_{1,2}, R_{1,2}(c_1, L). \quad (2\text{-}20)$$

For future use, we display at last the exact, structure-independent Hashin–Shtrikman (HS) bounds on the effective shear moduli [Milton 2002]:

$$(c_1\mu_1^{-1} + c_2\mu_2^{-1})^{-1} \le \mu_{1,2}^* \le c_1\mu_1 + c_2\mu_2 - \frac{c_1c_2(\mu_1 - \mu_2)^2}{c_1\mu_2 + c_2\mu_1 + \max\{K_1, K_2\}}. \quad (2\text{-}21)$$

Though not attainable on piecewise homogeneous composites, they serve as a benchmark to assess $\mu_{1,2}^*$ (see Section 5).

3. Problem formulation and solution procedure

We are now in a position to accurately rephrase the problem (1-1) of minimizing variation of the traction elastic stresses in complex-variable terms as follows.

Given the phases' elastic moduli and the volume fractions of a two-dimensional thin-grained elastic structure, to find the shape of a perfectly bonded foreign inclusion, which minimizes the contact stresses variation for either shear or torsion loading, we have:

$$V[P'(L)] \xrightarrow[L \in \Lambda]{} \min(K_1, K_2, \mu_1, \mu_2, c_1). \quad (3\text{-}1)$$

Maximization of either of the effective shear moduli,

$$\mu_{1,2}^*(L) \xrightarrow[L \in \Lambda]{} \max(K_1, K_2, \mu_1, \mu_2, c_1), \tag{3-2}$$

will also be studied in parallel with (3-1). In order to save computational effort, we additionally suppose that the admissible set Λ contains no concave curves, which are most likely not promising for optimization.

As already noted in Section 1, both problems have markedly different solutions with the attainable μ^*-maxima falling rather short of the upper HS bound.

In light of these considerations, our objective is to quantitatively illustrate the described situation by optimizing both criteria for a representative data set. In doing so, we intend to obtain the evolution of the V-optimal solutions with increasing c_1 and to compare them with their μ^*-optimal counterparts. Unlike in the equistress case, here only a numerical solution of (3-1) and (3-2) is available.

The computational size of this shape optimization problem is halved by the relations derived in Section 2, the loads (2-8), the boundary stresses (2-16) and (2-17), and the effective moduli (2-18), are free from $\chi_1(z)$ and from the doubly periodic part $\eta(z)$ of $\chi_2(z)$ in (2-4). Because of their analyticity, both functions may also be eliminated from the boundary conditions (2-15) of the DEP [Vigdergauz 2013]. Actually, $\chi_1(z)$ and $\eta(z)$ are needed only to find the stresses strictly inside the phases, which is outside of our current scope.

In the previous papers [Vigdergauz 2012a; 2013] we used this feature to develop a simple and fast computational tool for stochastic shape optimization in two-dimensional elastostatics. The experience gained from a series of applications provides strong grounds to believe that here it will do as well. Because the tool is detailed in the above-mentioned articles, now we only briefly sketch its basic constituents for convenient reference. They include: (A) an enhanced direct solver adapted specially for KM potentials, (B) an economical shape encoding scheme, and (C) a standard genetic algorithm search for the optimum.

(A) By eliminating $\chi_1(z)$ and $\eta(z)$, the initial DEP is equivalently transformed into an infinite system of linear algebraic equations in the quasiperiods D_1, D_2, R_1, and R_2, and the φ-coefficients $\{d_{1,2}\}$ from (2-10). In numerical practice, the system is truncated at a finite size N with real entries. They come as regular integrals over L with the integrands composed of the basic functions in (2-10) and their conjugates and derivatives.

(B) Such integrals are commonly calculated using quadratures over a number of points along the discretion path in the parameter space, the choice of which is important for the numerical efficiency of the optimization as a whole. To this end, we propose to employ a finite-term conformal mapping of the exterior of the unit circle γ onto the square-symmetric inclusion shape L [Ahlfors 1978]:

$$t = \Omega(\tau) = C\left(\tau + \sum_{q=1}^{Q} a_{4q-3}\tau^{-4q+3}\right), \quad t \in L, \quad \tau = \exp i\theta \in \gamma, \quad 0 \le \theta \le 2\pi, \tag{3-3}$$

which straightforwardly incorporates geometrical constraints [Vigdergauz 2012b]. Particularly, the assumed shape convexity is explicitly enforced in the current terms as [Pólya and Szegő 1972]

$$\operatorname{Re} \frac{\tau \Omega''(\tau)}{\Omega'(\tau)} > -1, \quad \tau \in \gamma. \tag{3-4}$$

An arbitrary multiplier C is used for scaling the shape to a given volume fraction c_1 of the inclusion. In fact, the proposed conformal-mapping parametrization replaces the initial searching space with its $(Q+1)$-dimensional subspace, ordered in the sense that the higher coefficient a_{4q-2} is, the less impact it has on the shape. This scheme dramatically reduces the running time and gives a better convergence rate than the usual nodal representation. It also allows us to compute the boundary integrals through the same set of points $h_m \in \gamma$, $m = 1, 2, \ldots, M$, along the unit circle independently of the actual shape L.

(C) A gradientless genetic algorithm (GA) approach which employs the mapping coefficients $\{a_{4q-2}\}$ as design variables bounded by the required mapping uniqueness [Ahlfors 1978], $-(4q-3)^{-1/2} \leq a_{4q-3} \leq (4q-3)^{-1/2}$. The growing popularity enjoyed by GAs is mostly due to their simplicity and practically proven ability to find the global or near-global optimum in difficult high-dimensional problems, especially, where the search space is not well understood. Another strong GA feature is implementation flexibility. In effect, only the shape-encoding procedure and the fitness-evaluation scheme specifically configure the basic GA for a current purpose.

4. Numerical scheme verification

Before performing the simulations, the accuracy of the built-in deterministic solver of the KM potentials needs to be estimated by comparing against available data from the literature.

A good example is the case of a square array of hard circular disks ($K_1 = 225$, $\mu_1 = 135$) in a soft matrix ($K_2 = 3\frac{1}{3}$, $\mu_2 = 1$) whose effective shear moduli $\mu^*_{1,2}$ from (2-18) are computed in [Greengard and Helsing 1998] with the highest accuracy by solving an integral equation of Sherman–Lauricella type [Muskhelishvili 1975]. Comparison with our results (Table 1) shows remarkably good agreement almost up to the percolation threshold $c_1 = \pi/4 \approx 0.785398\ldots$. The reason for this is that the circle has no angular points which may not be exactly mapped by the finite-term approximation (3-3).

This is in contrast to, say, the exact FEM representation, actually used by [Berggren et al. 2001] to compute the effective moduli of an elastic plate with a square lattice of square holes ($\mu_1 = 0$) for different

μ^*_1	$c_1 = 0.3$	$c_1 = 0.5$	$c_1 = 0.78$	$c_1 = 0.785$
GH	1.9415606008	3.7984374034	33.0679995249	41.5392409243
Current	1.941560601	3.7984374034	33.06798462	41.52200211
Relative error	2.053×10^{-11}	3.488×10^{-12}	4.507×10^{-7}	4.150×10^{-4}
V-criterion	2.602	2.752	9.944	15.745
μ^*_2	$c_1 = 0.3$	$c_1 = 0.5$	$c_1 = 0.78$	$c_1 = 0.785$
GH	1.5410983175	2.1743265379	14.6242590661	27.277092151
Current	1.541098318	2.174326538	14.62424051	27.05524626
Relative error	-1.260×10^{-11}	-1.293×10^{-12}	1.269×10^{-6}	8.133×10^{-3}
V-criterion	1.849	1.719	5.701	14.656

Table 1. A square array of hard disks in a soft matrix: comparison of the $\mu^*_{1,2}$ values obtained by different methods at different values of the inclusion volume fraction c_1. The corresponding V-criteria are also added for completeness. Data from [Greengard and Helsing 1998] is labeled by GH.

q	1	2	3
d_{4q-1}	-0.159082817	$1.4840715179 \times 10^{-2}$	$-3.756551076 \times 10^{-3}$
q	4	5	6
d_{4q-1}	$1.355021822 \times 10^{-3}$	$-4.465339808 \times 10^{-4}$	$1.194202545 \times 10^{-4}$

Table 2. The side-straightening coefficients of the circle-to-square conformal mapping.

values of their volume fraction. Before reproducing these results with the current approach, we have to find the mapping coefficients $\{d_{4q-1}\}$ from (3-3). In the current context, the most relevant way to do this is again a genetic algorithm minimizing the *V*-criterion:

$$\sum_{i=0}^{n} |\mathrm{Im}(t_{i+1}) - \mathrm{Im}(t_i)| \xrightarrow[\{d_m\}]{} \min, \quad \{t_i\} \in L, \quad 0 \leq \arg(t_i) \leq 45°, \tag{4-1}$$

at a given area of the square for nonconcave curves (3-4). The criterion (4-1) straightens the segment of square-symmetric shape which corresponds to the right half of the square. The resultant coefficients for $Q = 6$ and the *V*-optimal shape are given in Table 2 and Figure 1, respectively.

For clarity, it should be pointed out that the *V*-criteria (3-1) and (4-1) are divorced from each other. The latter is a pure conformal approximation of an isolated given shape and hence does not include the KM direct solver. It may find further use in similar situations.

Table 3 compares the FEM-obtained values of μ_1^*-related constants (2-20) from [Berggren et al. 2001] to their KM counterparts. Here the relative errors are several orders of magnitude worse than those for the circle. This gap may not completely account for the rounded square corners as the FEM-related results correspond to *smaller* values of μ_1^*. Actually, it should be the reverse: they are found as the minimum of a
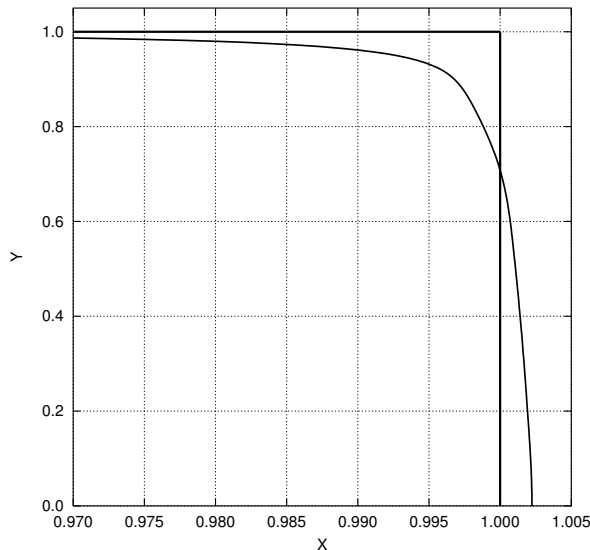
Figure 1. The six-term equiarea mapping of a unit square. The maximum deviation, $\delta \approx 0.0283$, occurs at the square's vertex

	$c_1 = 0.1$	$c_1 = 0.3$	$c_1 = 0.5$	$c_1 = 0.7$	$c_1 = 0.9$
BLMS	0.179394	0.563755	1.165734	2.519723	9.202034
Current	0.178934	0.561895	1.160867	2.508157	9.161075
Relative error	2.57×10^{-3}	3.299×10^{-3}	4.175×10^{-3}	4.590×10^{-3}	4.451×10^{-3}

Table 3. The c_1-dependent constant $R_1(c_1)$ from (2-20) for a square array of square holes in a matrix. Values are shown for the FEM of [Berggren et al. 2001] (denoted BLMS) and the KM solver.

variational problem [Berggren et al. 2001] and hence remain always *larger* than the exact values. In other words, the FEM estimate seems too conservative, as noted by the authors themselves. This solver's accuracy is, however, acceptable for our purposes. Possibly excessive smoothing of angular points through neglecting the high-order coefficients is counteracted by the integral nature of the V-criterion.

Furthermore, since probabilistic computations are nonexplicit and involve heuristic parameters, the proposed GA-optimization approach should be carefully calibrated by multiple test runs on real data. The proximity to the true extremum can be only estimated through the internal convergence of the results for problem size parameters successively increasing from the initial values $Q = 5 \div 7$, $N = 16 \div 48$, and $M = 360$, for varying c_1. These choices for further computations are based on our experience in the previous studies [Vigdergauz 2012a; 2012b; 2013]. In the current simulations the V-optimum relative deviations induced by doubling each size remain typically less then 0.6%, providing an acceptable compromise between accuracy and computational cost. For eliminating GA-related stochastic noise, all output data were computed several times, randomly starting each optimization process and stopping the evolution after a rather large number of iterations, when the fitness is deemed to converge.

5. Numerical results

The conducted GA simulations aim to numerically find the optimum, by (3-1) and (3-2), in the representative interval of the inclusion volume fraction c_1 at given phases' moduli. In order to make the results more conclusive, we present, for comparison, four distinctive cases, namely the interchanged pairs of soft inclusions/hard matrix and hard inclusion/soft matrix, each under either shear or torsion load. The local moduli values are borrowed from [Greengard and Helsing 1998], as given in the previous section. The graphed results show the c_1-dependent evolution of the V- and $\mu_{1,2}^*$-optimal inclusion shapes, the corresponding $\mu_{1,2}^*(c_1)$ values, and, finally, the stress distributions along the V-optimal interfaces. For correct comparison we kept the same GA parameter values for all observations.

Figure 2 presents the computed $V(c_1)$-optima for the chosen cases. It is of interest that the hard inclusion demonstrates the decreasing dependence of V on c_1. As we shall see below, this is primarily due to narrowing the interval (1-3) between the extrema of the case-dominating tangential tractions $\sigma_{n\theta}$ with increasing c_1 rather than due to smoothing.

Figure 3 shows the $\mu_1^*(c_1)$ and $\mu_2^*(c_1)$ maxima against their V-optimal counterparts and those of the circular inclusions, all within the HS bounds (2-21).

Essentially, even the $\mu_{1,2}^*$ maxima appear to be rather far from the upper HS bound. This is particularly true of the second modulus μ_2^*. Similar μ^*-optimization results have been obtained in [Vigdergauz 2001] for a more simple limiting case of a perforated structure ($\mu_1 = 0$). Furthermore, V-optimization
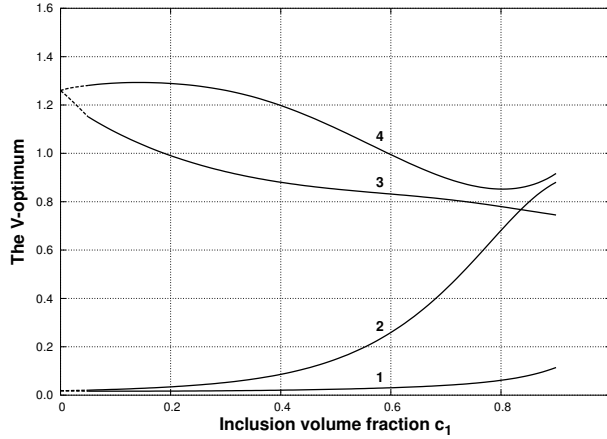
Figure 2. The $V(c_1)$-optimum for the soft (1 and 2) and hard (3 and 4) inclusions under shear and torsion, respectively. The limiting values $V(0)$ (the dashed lines) are extrapolated from the computed interval $c \in [0.05; 0.9]$.
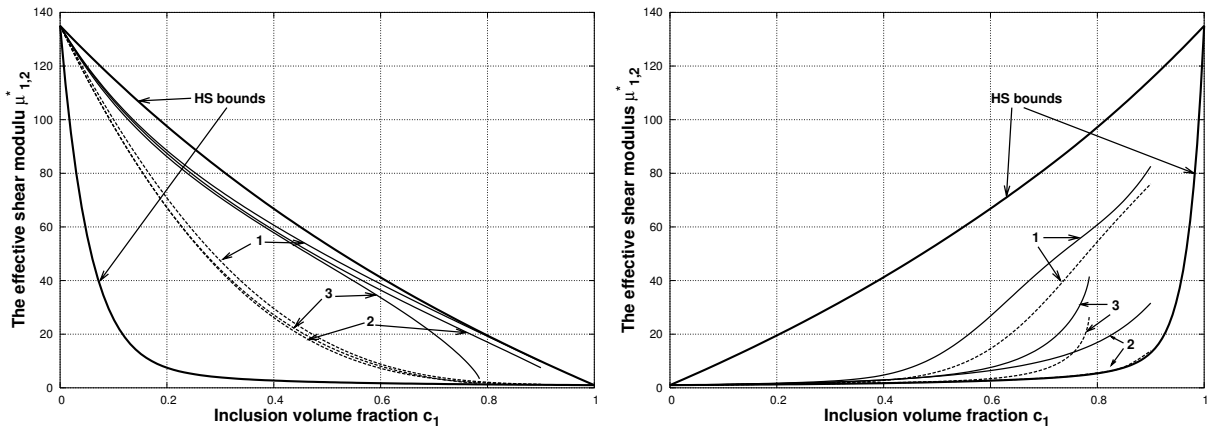

Figure 3. The soft (top) and hard (bottom) inclusions, for the effective shear moduli $\mu_1^*(c_1)$ and $\mu_2^*(c_1)$ (the dashed lines) within the HS bounds: optimum (1) and V-related values (2). The moduli for the circular inclusion (3) are also added for comparison.

is performed at the sacrifice of substantially decreased shear effective moduli, especially for the hard inclusion where the V-related modulus μ_2^* lies close to the HS *lower* bound. Moreover, in this case the V-related effective shear moduli are significantly less than even those for the circle (Figure 3, bottom). This is accounted for by affecting the V-performance of the inclusion shapes, as shown in Table 4. Since in both cases the tractions are monotone functions of the angle θ in the irreducible interval $[0, \pi/4]$ (see Figure 6 on page 101), V-optimization acts here by drastically diminishing their tangential components at the significant expense of much lower normal stresses, which enter into the criterion (1-2) with the same weight. Conceivably, the case-dependent weights for either component might improve the numerical sensitivity of the optimization scheme. This complication is, however, beyond the scope of this paper.

	V	μ_2^*	$\max(\sigma_{nn}(\theta))$	$\max(\sigma_{n\theta}(\theta))$
V-opt	0.801	4.342	0.373	0.634
Circle	1.205	6.654	0.190	1.544
Difference (%)	50.4	-53.2	49.0	-143.3

Table 4. The hard inclusion under torsion at $c_1 = 0.75$: comparison of the numerically obtained V-optimal values of K_e with those for the circular shape. The relative difference between each pair of counterparts with respect to the former is also added for convenience. Conforming with the symmetry relations (5-1b), $\min(\sigma_{nn}) = \min(\sigma_{n\theta}) = 0$.

Of special interest are the V and μ^*-optimal square-symmetric shapes compared in Figure 4 for discrete values of c_1. In all instances, the μ^*-optimal inclusion shapes tend, as expected, to form nearly straight segments connecting distinct angular points. Their favorable role in maximizing the shear moduli
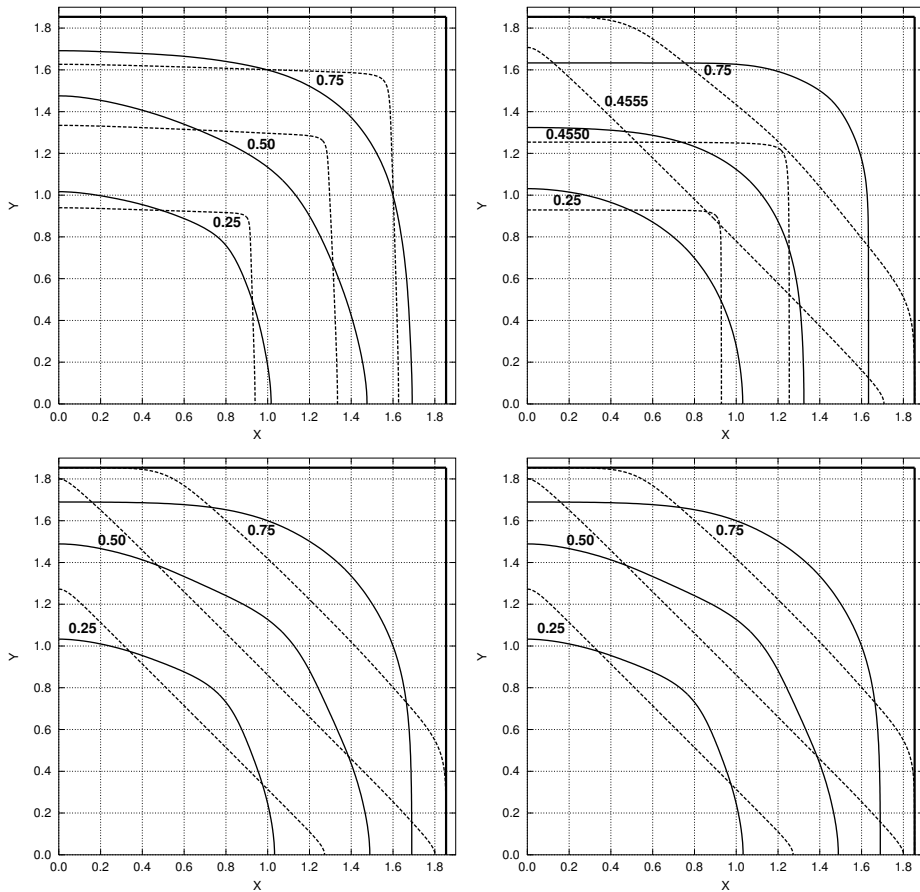
Figure 4. The soft (left) and the hard (right) inclusions under shear (the top two graphs) and torsion (the bottom two): evolution of the V- and μ^*-optimal (the dashed lines) shapes with increasing volume fraction c_1.

was first numerically observed by Vigdergauz and Cherkayev [1986] and later analyzed in more depth [Cherkaev et al. 1998] for the simplest case of an isolated hole in a shear-loaded infinite plane. On the contrary, due to its smoothing nature, V-optimization rounds the inclusion shape. Furthermore, at any c_1, the μ_1^* and μ_2^*-optimal soft inclusions differ from each other by rotation about the origin through $45°$ as caused by the different principal directions of the shear and torsion trial loads. For the μ^*-optimal holes this fact was indicated in [Vigdergauz 2001].

The μ_1^*-optimal hard inclusion behaves more complicatedly than the soft. It experiences a sudden rotation by $45°$ when evolving through the interval $c_1 \in [0.4550; 0.4555]$ (see the top right graph in Figure 4). This puzzling observation should be verified independently by other methods.

Finally, Figures 5 and 6 illustrate the angular distribution of the tractions and the induced hoop stresses along the irreducible part $0 \le \theta \le 45°$ of the V-optimal interface. The symmetry relations (2-14) give the following locations of the distributions' zeros:
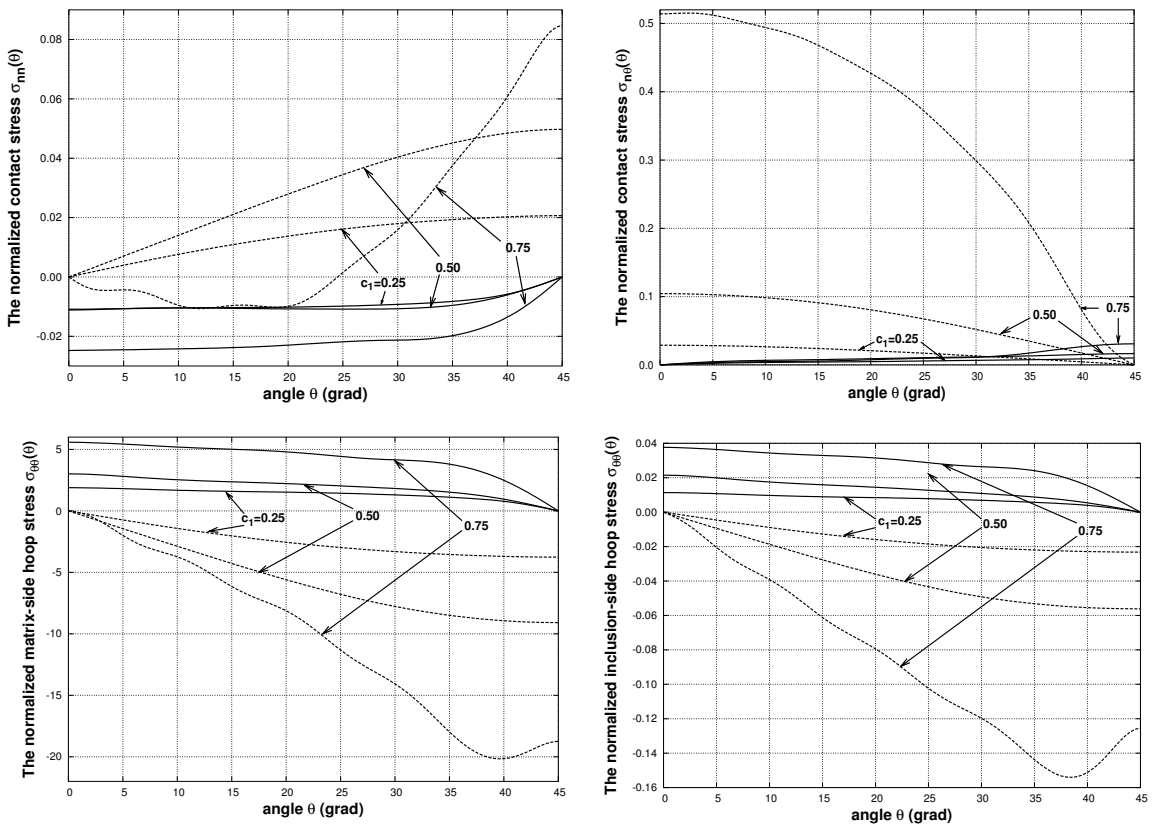
Figure 5. The boundary stresses for the V-optimal soft inclusion under shear and torsion (the dashed lines) for varying inclusion volume fraction c_1: the normal contact traction (top left), tangential contact traction (top right), matrix-side hoop stress (bottom left), and inclusion-side hoop stress (bottom right).
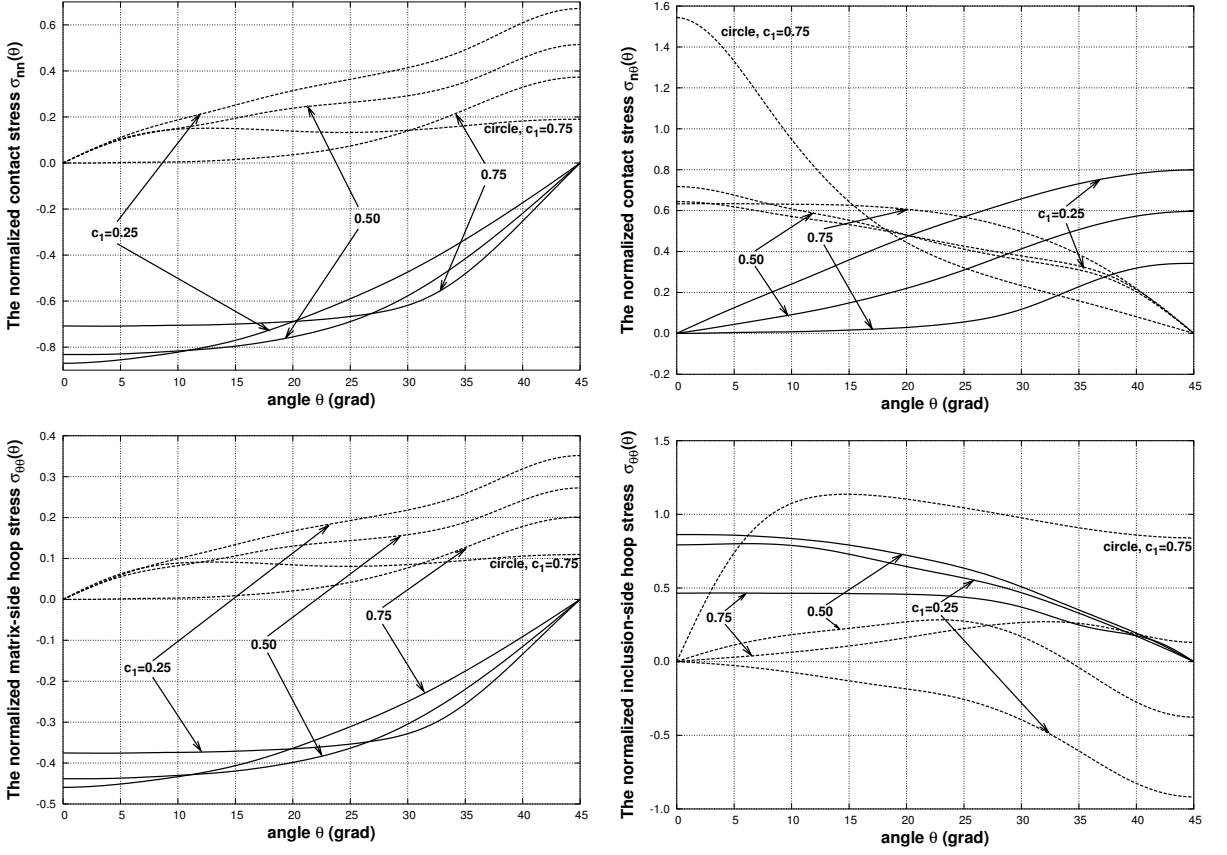
Figure 6. The boundary stresses for the *V*-optimal hard inclusion under shear and torsion (the dashed lines) with change in the inclusion volume fraction c_1: the normal contact traction (top left), tangential contact traction (top right), matrix-side hoop stress (bottom left), and inclusion-side hoop stress (bottom right). Data for the circular hole at $c_1 = 0.75$ under torsion are also added for comparison.

$$\sigma_{nn}(\pi/4) = \sigma_{n\theta}(0) = \sigma_{\theta\theta}^{(m)}(\pi/4) = \sigma_{\theta\theta}^{(i)}(\pi/4) = 0 \quad \text{for shear,} \tag{5-1a}$$

$$\sigma_{nn}(0) = \sigma_{n\theta}(\pi/4) = \sigma_{\theta\theta}^{(m)}(0) = \sigma_{\theta\theta}^{(i)}(0) = 0 \qquad \text{for torsion.} \tag{5-1b}$$

It should be borne in mind that the angle $\theta = \arctan(y/x) : t = x + iy \in L$ is measured in the physical plane rather than around the auxiliary unit circle γ. From these figures, one sees that none of the patterns show high-frequency oscillations. This is also true for the hoop stresses $\sigma_{\theta\theta}(\theta)$, which are not involved explicitly in the *V*-smoothing process.

In most cases, the boundary stresses are monotonic functions of the angle θ. The only exceptions are provided by the torsion for all stresses around the soft inclusion at $c_1 = 0.75$ and for the hard inclusion-side hoop stresses at any c_1. Curiously the extremal values of the normal and tangential tractions around the hard inclusion under torsion and shear, respectively, decrease with increasing c_1 (see Figure 6). Both features are not *V*-specific since they also take place for the circle (not shown for better visibility).

6. Summary and future applications

The numerical *V*-optimization of the interface tractions is now extended to planar grained structures under shear and torsion loads. As explained in Section 1, this loading case merits separate attention. The results obtained attest to the general applicability of the proposed *V*-criterion. Computationally, they are rather accurate, marking a sharp contrast with the biaxial mode, where the equistress principle permits one to simultaneously saturate the structurally independent HS upper K^* bound and the *V*-optimum by the same inclusions shapes. For clarity, we summarize the basic distinctions as follows.

- The *V* and μ^*-optimal inclusions significantly differ from each other in their shapes and orientations. The degree of dissimilarity depends on all the parameters involved: the load type, the relative inclusion rigidity, and its volume fraction.

- As a result, the corresponding shear moduli appear to be rather different, with the maximum being far from the upper HS bound. For bimaterial grained structures its unattainability was first proved by Allaire and Aubry [1999], if not earlier. Now some nontrivial quantitative characteristics of this phenomenon are also provided.

- Finally, the above-noted (see Section 5) dramatic rotation of the μ_1^*-optimal hard inclusion in passing the point $c_1 \approx 0.45525$ is well worth a further look and independent corroboration.

These observations stimulate similar investigations for *V*-optimal structures with badly ordered phases or with macroisotropy. In the latter case, it is of special interest to compare the numerical results with the corresponding phase-interchange analytical relations deduced by Gibiansky and Torquato [1996]. We hope to pursue both issues in further publications. It would also be interesting to study the *V*-criterion's performance for the weighted sums in (1-1), as mentioned in Section 5. Due to the lack of analytical results, it would be prudent here to use a straightforward, numerical trial-and-error approach.

References

[Abramowitz and Stegun 1965] M. Abramowitz and I. A. Stegun, *Handbook of mathematical functions, with formulas, graphs, and mathematical tables*, National Bureau of Standards Applied Mathematics Series **55**, Dover, New York, 1965.

[Ahlfors 1978] L. V. Ahlfors, *Complex analysis*, 3rd ed., McGraw-Hill, New York, 1978.

[Allaire and Aubry 1999] G. Allaire and S. Aubry, "On optimal microstructures for a plane shape optimization problem", *Struct. Opt.* **17**:2-3 (1999), 86–94.

[Berggren et al. 2001] S. A. Berggren, D. Lukkassen, A. Meidell, and L. Simula, "On stiffness properties of square honeycombs and other unidirectional composites", *Compos. Part B-Eng.* **32**:6 (2001), 503–511.

[Cherkaev et al. 1998] A. V. Cherkaev, Y. Grabovsky, A. B. Movchan, and S. K. Serkov, "The cavity of the optimal shape under the shear stresses", *Int. J. Solids Struct.* **35**:33 (1998), 4391–4410.

[Gakhov 1966] F. D. Gakhov, *Boundary value problems*, Pergamon, Oxford, 1966. Reprinted Dover, New York, 1990.

[Gibiansky and Torquato 1996] L. V. Gibiansky and S. Torquato, "Phase-interchange relations for the elastic moduli of two-phase composites", *Int. J. Eng. Sci.* **34**:7 (1996), 739–760.

[Greengard and Helsing 1998] L. Greengard and J. Helsing, "On the numerical evaluation of elastostatic fields in locally isotropic two-dimensional composites", *J. Mech. Phys. Solids* **46**:8 (1998), 1441–1462.

[Lukkassen et al. 2012] D. Lukkassen, A. Meidell, and K. Pettersson, "An elementary proof of the Vigdergauz equations for a class of square symmetric structures", preprint, 2012. arXiv 1204.6419

[Milton 2002] G. W. Milton, *The theory of composites*, Cambridge Monographs on Applied and Computational Mathematics **6**, Cambridge University Press, 2002.

[Muskhelishvili 1975] N. I. Muskhelishvili, *Some basic problems of the mathematical theory of elasticity*, 2nd ed., Noordhoff, Leyden, 1975.

[Natanson 1955] I. P. Natanson, *Theory of functions of a real variable*, Frederick Ungar, New York, 1955.

[Pólya and Szegő 1972] G. Pólya and G. Szegő, "Some geometrical aspects of complex variables, problem 108", pp. 125–132 in *Problems and theorems in analysis, I: Series, integral calculus, theory of functions*, edited by G. Pólya and G. Szegő, Die Grundlehren der mathematischen Wissenschaften **193**, Springer, New York, 1972.

[Vigdergauz 1999] S. Vigdergauz, "Complete elasticity solution to the stress problem in a planar grained structure", *Math. Mech. Solids* **4**:4 (1999), 407–439.

[Vigdergauz 2001] S. B. Vigdergauz, "The effective properties of a perforated elastic plate: Numerical optimization by genetic algorithm", *Int. J. Solids Struct.* **38**:48-49 (2001), 8593–8616.

[Vigdergauz 2012a] S. Vigdergauz, "Stress-smoothing holes in an elastic plate: From the square lattice to the checkerboard", *Math. Mech. Solids* **17**:3 (2012), 289–299.

[Vigdergauz 2012b] S. Vigdergauz, "Stress-smoothing holes in an elastic plate: The triangular checkerboard lattice of low symmetry", *Math. Mech. Solids* **17**:6 (2012), 652–665.

[Vigdergauz 2013] S. Vigdergauz, "A generalization of the equi-stress principle in optimizing the mechanical performance of two-dimensional grained composites", *Math. Mech. Solids* **18**:4 (2013), 431–445.

[Vigdergauz and Cherkayev 1986] S. B. Vigdergauz and A. V. Cherkayev, "A hole in a plate, optimal for its biaxial extension-compression", *J. Appl. Math. Mech.* **50**:3 (1986), 401–404.

SHMUEL VIGDERGAUZ: `vigd1805@013.net`
Research and Development Division, The Israel Electric Corporation Ltd., P.O. Box 10, 1, Nativ-ha-Or, 31000 Haifa, Israel

JOURNAL OF MECHANICS OF MATERIALS AND STRUCTURES

msp.org/jomms

Founded by Charles R. Steele and Marie-Louise Steele

Cover photo: Ev Shafrir

Journal of Mechanics of Materials and Structures